

Virtual Electrode Design for Lithium-Ion Battery Cathodes


Jochen Joos,* Alexander Buchele, Adrian Schmidt, André Weber, and Ellen Ivers-Tiffée

Microstructural characteristics of lithium-ion battery cathodes determine their performance. Thus, modern simulation tools are increasingly important for the custom design of multiphase cathodes. This work presents a new method for generating virtual, yet realistic cathode microstructures. A precondition is a 3D template of a commercial cathode, reconstructed via focused ion beam/scanning electron microscopy (FIB/SEM) tomography and appropriate algorithms. The characteristically shaped micrometer-sized active material (AM) particles and agglomerates of nano-sized carbon-binder (CB) particles are individually extracted from the voxel-based templates. Thereby, a library of roughly 1100 AM particles and 20 CB agglomerates is created. Next, a virtual cathode microstructure is predefined, and representative sets of AM particles and CB agglomerates are built. The following re-assembly of AM particles within a predefined volume box works using dropping and rolling algorithms. Thereby, one can generate cathodes with specified characteristics, such as the volume fraction of AM, CB and pore space, particle-size distributions, and gradients thereof. Naturally, such a virtual twin is a promising starting point for physics-based electrochemical performance models. The workflow from the commercial cathode microstructure through to a full virtual twin will be explained and assessed for a blend cathode made of the two AMs, LiNiCoAlO₂ (NCA) and LiCoO₂ (LCO).

1. Introduction

The performance of a lithium-ion battery (LIB) cell is determined by the microstructural characteristics of its electrodes.^[1,2] Systematic studies on this complex relationship are of great value and demand to study a broad range of microstructures with different characteristics. A virtual design approach has, therefore, significant advantages over laboratory experiments, as it can be done much faster, more flexibly, and more precisely.^[3]

Dr. J. Joos, A. Buchele, A. Schmidt, Dr. A. Weber, Prof. E. Ivers-Tiffée
Institute for Applied Materials—Materials for Electrical and Electronic Engineering (IAM-WET)
Karlsruhe Institute of Technology (KIT)
Adenauerring 20b, 76131 Karlsruhe, Germany
E-mail: jochen.joos@kit.edu

 The ORCID identification number(s) for the author(s) of this article can be found under <https://doi.org/10.1002/ente.202000891>.

© 2021 The Authors. Energy Technology published by Wiley-VCH GmbH. This is an open access article under the terms of the Creative Commons Attribution-NonCommercial-NoDerivs License, which permits use and distribution in any medium, provided the original work is properly cited, the use is non-commercial and no modifications or adaptations are made.

DOI: 10.1002/ente.202000891

The latter point is of special importance, because one of the decisive advantages of numerical studies is that virtual structures can be produced in such a way that only one parameter is changed, whereas the other parameters are kept constant. Then, microstructure–performance relationship becomes predictable in combination with physics-based electrochemical models (homogenized Newman-type models and, preferably, spatially resolved 3D models^[4–6]).

LIB cathodes typically consist of the three main phases: 1) active material (AM); 2) carbon-binder (CB) agglomerates (agglomerates of many nanometer-sized carbon black particles + binder material, added to increase the electronic conductivity of the cathode); and 3) pore phase (which is soaked with liquid electrolyte during operation). Some cathodes even have two or more different AMs and are, therefore, called blend cathodes. In the literature, there are different approaches for generating virtual cathodes. Most of the approaches use simplified particle shapes to approximate the complex real shape of the AM particles, e.g., spheres,^[7]

ellipsoids,^[8,9] or more arbitrarily shaped particles.^[3,10,11] Other approaches try to capture the complex microstructure in more detail through complex stochastic models.^[3,12] The disadvantage is that they are hard to parametrize, and it is difficult to systematically or precisely vary the microstructural characteristics.^[12] Simplified structures can be used to study basic phenomena, but they fail to reproduce a true image of AM particles and CB phase assembled in a technical cathode.

In this work, the generation of a virtual twin consists of five basic model steps, which have to be performed sequentially. First, commercial cathodes are reconstructed using focused ion beam/scanning electron microscopy (FIB/SEM) tomography and appropriate algorithms delivering a 3D digital template.^[13–15] Second, the individual AM particles and CB agglomerates within the 3D data are cut out using a newly developed approach based on morphological operations. Thereby, a library list is filled with individually shaped AM particles (roughly 1100) and large CB agglomerates comprising of several hundreds of primary CB particles (20). Model steps 1 and 2 are prerequisites for the generation of a variety of virtual cathode structures.

The virtual structure generator is based on a matrix grid that represents the voxel-based microstructure (voxel = volumetric pixel) and applies three sequential steps. Model step 3: definition of material portions and particle-size distributions. Model step 4: sequential placement of AM particles in a dimension-specified

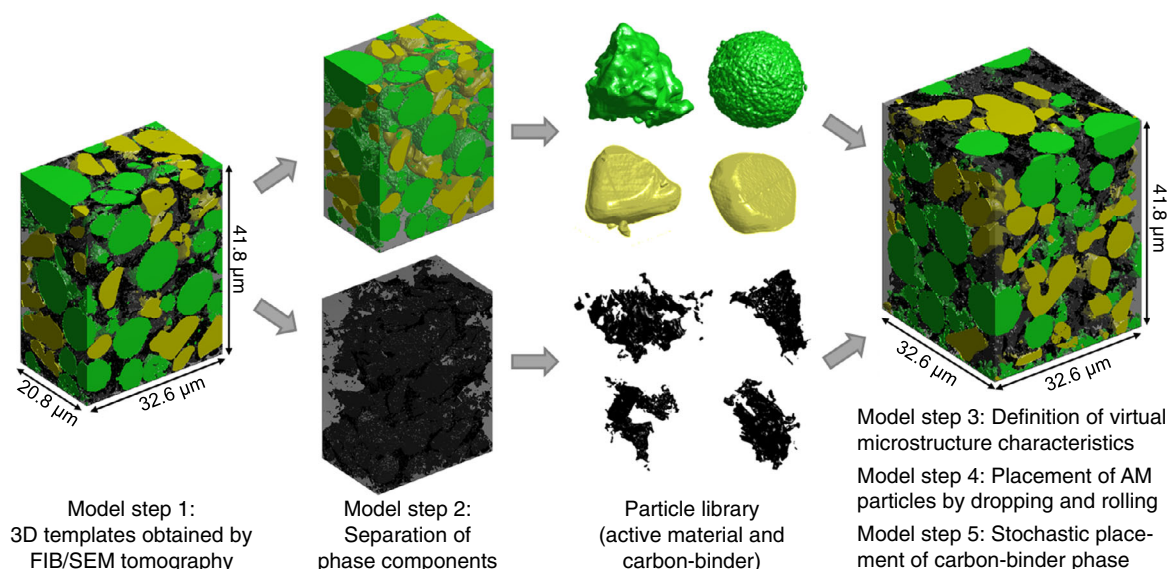


Figure 1. Workflow for generating virtual yet realistic microstructures: A 3D template is obtained from FIB/SEM tomography, from which the AM particles and CB agglomerates are extracted and stored in a library list. These particles and agglomerates are then used to generate virtual structures with predefined characteristics.

box by dropping and rolling. Model step 5: stochastic placement of CB agglomerates into the remaining pore space. The entire workflow is shown in **Figure 1**, and Section 2 and 3 detail all model steps.

2. Particle Library

The following sections explain the workflow within model steps 1 and 2, starting with a genuine 3D template of a real cathode structure and ending with a library list of separated individually shaped AM particles and CB agglomerates.

2.1. Model Step 1: 3D Templates Obtained by FIB/SEM Tomography

Most common, microstructure characteristics of battery cathodes are analyzed by FIB/SEM tomography and then joined together to a 3D reconstruction with the help of suitable algorithms. In this way, the features of the AM phase(s), the carbon black (+binder material) phase, and the pore phase are recorded quantitatively, and information on their individual characteristics becomes accessible. In recent years, our group first analyzed LiFePO_4 ,^[14] followed by LiCoO_2 (LCO), LiNiCoAlO_2 (NCA), and two NCA/LCO blend cathodes gained from commercial high-energy and high-power cathode sheets.^[15] The data sets of the latter four cathodes are the basis for establishing the particle library; see in the following. Other groups have reported LCO (e.g., Wilson et al. and Malavé et al.^[1,16] without consideration of the CB phase, or Hutzenlaub et al.^[17] considering all phases), or LiMn_2O_4 (LMO).^[18] More recently, our group published FIB/SEM tomography of four LiNiCoMnO_2 (NMC) cathodes.^[19] However, the entire procedure will be summarized concisely.

The FIB procedure uses an FIB to perform nanoscale sectioning of a sample, which is simultaneously imaged by the electron beam of an SEM. Sequential milling and imaging yield a serial set of consecutive SEM images of the analyzed structure. By stacking the 2D SEM images within a 3D space and aligning the SEM images, a 3D reconstruction is derived.^[13] This 3D data set of voxels contains essential microstructure parameters, such as 1) material fractions x_i of all phases i ; 2) surface area densities a_i ; 3) tortuosities τ_i ; or 4) particle and pore shapes, sizes, and distributions and their average values.

A very important aspect regarding the accuracy of the calculated parameters is the resolution of the SEM images. A minimum of ten pixels for the particle diameter of each particle is essential for, e.g., the accurate determination of the surface area a_i .^[20] The image distance (spacing between the images; z-direction), as well as the cross-sectional resolution (pixel size of SEM images; x–y plane), has, therefore, been chosen between 30 nm and 50 nm for the cathodes, based on the expected particle sizes of the AM particles. To characterize statistically representative volumes,^[20] the 3D data sets were as large as $19.5\text{--}28.3 \times 10^3 \mu\text{m}^3$ or $57\text{--}83 \times 10^6$ voxel (voxel sizes between 30 and 50 nm) for all four investigated cathodes. **Figure 2** shows an exemplary set of consecutive SEM images alongside with its final 3D reconstruction. The 3D volume shows a section ($32.6 \times 20.8 \times 41.8 \mu\text{m}^3$) of the commercial high-energy cathode LCO/NCA-E.

2.1.1. Algorithms

The region growing segmentation algorithm assigns all areas of the same phase (AM, CB, and porosity) to the same index value in the 3D reconstruction data.^[21] Due to the weak contrast between NCA and LCO in the blend cathodes, all these particles are recognized as one joint AM. We inspected all consecutive 2D

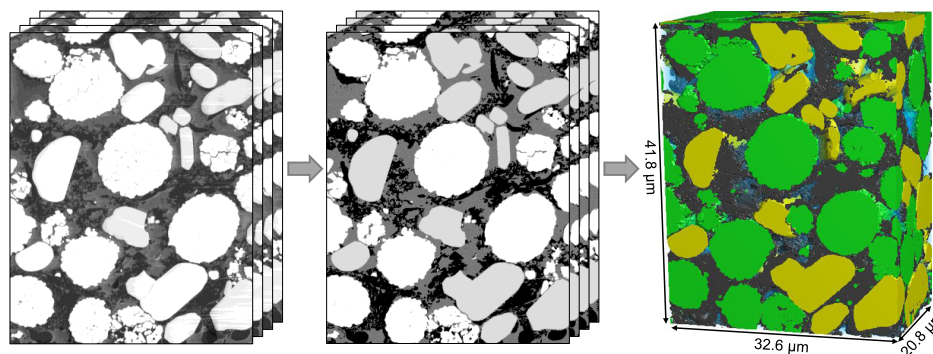


Figure 2. Workflow of FIB/SEM tomography shown for the template NCA/LCO-E cathode: The consecutive 2D SEM raw images are first stacked and aligned (left) and then segmented (middle) into the phases: 1) AM phases (green and yellow); 2) CB phase (black); and 3) pore phase (filled with electrolyte during operation) (right).

SEM images and selected manually between NCA and LCO particles relying on their characteristic particle shapes. This step was time-consuming, but indispensable. Therefore, we are currently working on a new segmentation algorithm using neuronal network. First results are promising; more than 95% of the particles are automatically assigned correctly.

Now, the material fractions x_i are calculated by simply dividing the number of voxels assigned to a specific phase i by the total number of voxels. The surface areas are calculated using the marching cube algorithm, which approximates the surface area using the information of eight neighboring voxels.^[22] The particle- and pore-size distributions are calculated on basis of the Euclidean distance transform (EDT), which is described in detail in the previous studies.^[23,24] The tortuosity is calculated by solving the transport equation directly on the 3D data obtained from FIB/SEM tomography^[13,20] using software developed by Ender et al.,^[24] which can cope with a 3D data set of over 900 million voxels, or using the software GeoDict (Math2Market, Kaiserslautern, Germany). The specification data of the four commercial LIB cathodes analyzed here as well as the sizes of the reconstructed volumes are shown in **Table 1**. More information is available in the previous study.^[15]

For executing the next model steps, all four data sets were resampled to a uniform voxel size of 70 nm, which only slightly changed the microstructural parameters of the structures.

2.2. Model Step 2: Separation of Phase Components

This section describes the iterative process of picking the individual particles of NCA, LCO, and CB phase out of the all-embracing 3D reconstruction.

The AM particles are for the most part in direct contact with each other, and sometimes deformed by tape calendaring. A splitting process is indispensable to receive single, individual particles. For simplification, the CB phase is deleted, and only the AM phase remains in the voxel-based volume. More precisely, the pore as well as the CB phase is assigned to the background, whereas the AM is assigned as foreground.

The contact areas between the individual particles are opened by two morphological operations. The *erode* operation shrinks the AM phase until the interconnection disappears. The degree of shrinkage is determined by a parameter that defines how many voxel layers should be deleted, starting from the border. The *dilate* operation enlarges the AM phase, which compensates for reducing the particle size in the *erode* operation. It is of importance that the *erode* operation is performed with a larger parameter than the *dilate* operation, but this leads to a small undefined area around the particles (indicated as a white area around the colored, separated particles in **Figure 3**). The refilling of these areas is described in the next paragraph. All separated parts detected after the opening process are assigned their own unique

Table 1. Specification of four commercial LIB cells with LCO, NCA, or NCA/LCO cathodes. FIB/SEM tomography was performed by Almar et al.^[15] the resulting 3D reconstruction data sets are used as cathode templates in this work.

Cells	NCA/LCO-E	NCA/LCO-P	LCO-E	NCA-P
Manufacturer	Kokam	Kokam	Sanyo	Sony
Format	Pouch	Pouch	18 500	18 650
Nominal Capacity (mAh)	560	350	1500	2600
Cathode AM	NCA-LCO	NCA-LCO	LCO	NCA
Cathode thickness [μm]	≈ 75	≈ 30	≈ 72	≈ 45
Reconstructed thickness [μm]	41.8	32.0	44.4	44.9
Volume [μm^3]	$32.6 \times 20.8 \times 41.8$	$30.0 \times 21.6 \times 32.0$	$24.0 \times 25.0 \times 44.4$	$16.8 \times 25.9 \times 44.9$
Voxel size raw data [nm]	35	40	50	30
Voxel size adapted [nm]	70	70	70	70

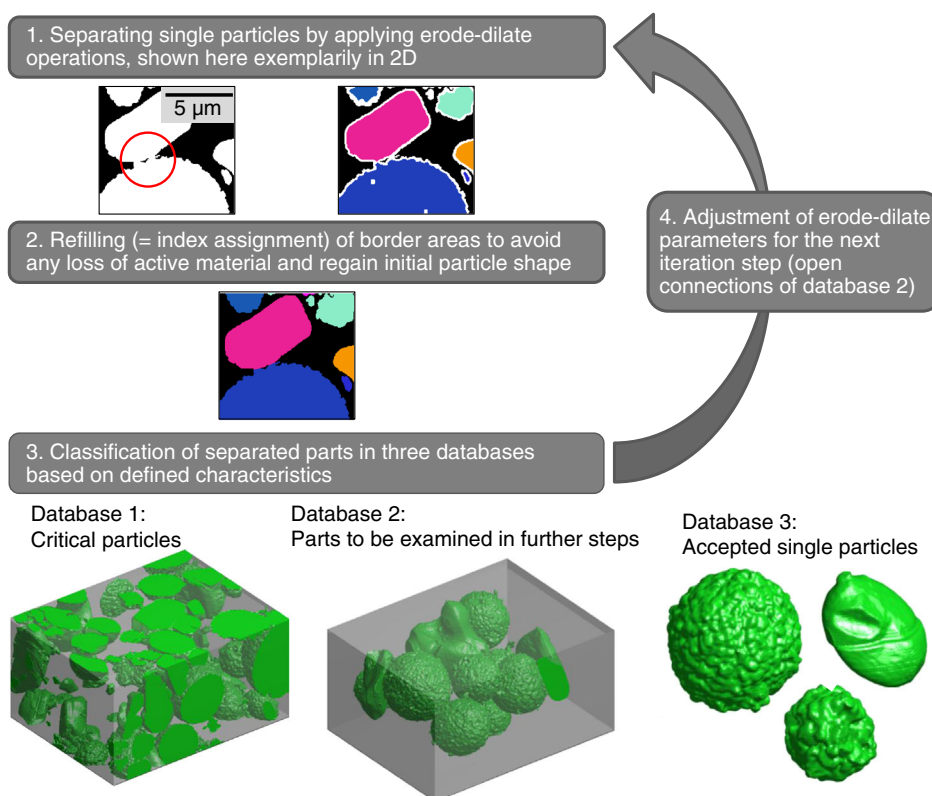


Figure 3. Phase and particle separation (example: NCA/LCO-E), illustrating the iterative process of the “opening” procedure: 2D schemes in the upper part visualizes the particle separation actually processed in 3D (steps 1 and 2); classified particles after interim separation (step 3): Database 1 “critical” particles, database 2 with particles need to be examined in a further step (4), and database 3 with “accepted” particles.

index in the 3D data set. The commonly used watershed algorithm was rejected, because it tends to over-segment the data.^[25]

The undefined white areas around the separated particles are refilled by considering surrounding information of the undefined voxels at the border areas. For these voxels, the indices of their directly adjacent neighboring voxels are considered. In case of one neighboring particle only, the considered voxel is assigned the same index. In case of more than one neighboring particle, an algorithm calculates the distance information between each voxel of the neighborhood and the temporary considered one as well as how often the indices occur. The considered voxel is assigned to the particle that has the most entries in the neighborhood and the shortest distance to these voxels. Since many neighboring voxels are still undefined in the first iteration, this process is repeated several times for each voxel until no more index changes occur.

As a matter of fact, no universal combination of *erode* and *dilate* parameters exist to separate all connections ideally in one step. The exact value for the two parameters of *erode* and *dilate* have to be chosen accordingly: Very weak connections can already be disconnected by applying *erode* with a value of two (and afterward *dilate* with a value of one), whereas for the strongest connections in our reconstructions, an *erode* operation with a parameter of 10 (followed by *dilate* with a parameter of 6) was necessary. Nevertheless, to prevent from over-segmentation and the loss of small AM particles by shrinking them to zero,

it is advantageous to start with a rather small erode–dilate combination and then gradually reinforce it. Therefore, an iterative routine has been developed to enable an automated separation of all particles of a reconstructed 3D volume. This procedure delivers, as shown in Figure 3, in each step, database 3 with successfully disconnected particles (“accepted single particles”), database 2 containing interconnected particles to be further examined in the next iterative loop, as also shown in Figure 4, and database 1 with critical particles, as described in the following.

Database 1 is comprised of particles that cannot be used for the final particle library. These particles are identified by meeting at least one of the following three criteria: 1) More than 10% of the particle surface is part of the boundary of the reconstruction. 2) The particle is at least twice as long in one direction as it is in the other directions. 3) The volume of a particle is less than a certain threshold, depending on the material.

The first criterion identifies incomplete particles at the boundaries, as at least one side of the particle is cut off at the edge of the reconstructed volume. The second criterion selects elements with an unusual elongated and narrow shape. These particles are most probably not AM particles, but more likely method-related artifacts of FIB/SEM tomography called “streaks” or “curtaining effect”.^[13,26] However, only very few parts (less than five) are sorted out due to the second criteria. The third criterion can be used if small particles (e.g., less than ten voxels) or splinters of AM should be excluded from the library.

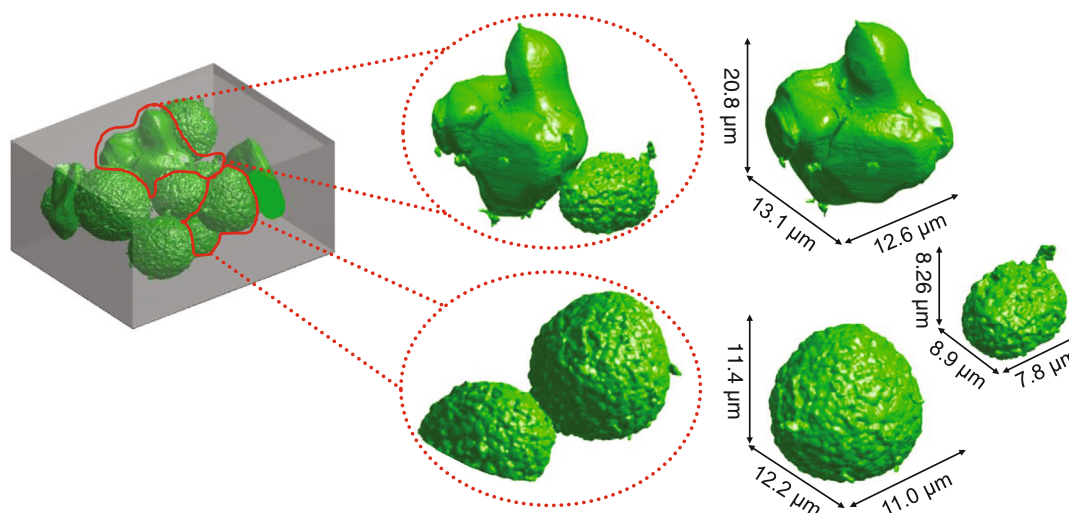


Figure 4. Connected AM network (database 2) after the first opening procedure (left) with two examples of connected particles (middle) and finally separated particles (right).

Database 2 contains particles still interconnected after the previous iteration of the erode–dilate operation. The following criteria have proved to automatically detect these agglomerates: 1) The considered part comprises more than a certain threshold of the total AM volume (e.g., 10% for small reconstructions or about 5% for very large ones). 2) The considered part is more than half the size of the 3D reconstruction in at least one dimension.

These interconnected particles have to undergo at least one further iterative separation step. Every iteration step contains an opening operation (erode–dilate), the refilling of border areas, and the classification procedure of the separated parts explained earlier.

Database 3 contains all particles, which do not meet any of the five criteria. They are labeled as “accepted” and added to the AM library. Figure 4 shows some of the accepted particles, which are suitable for creating realistic but virtual microstructures.

A further iteration step is necessary, until all particles are separated. For example, six iterative steps up to an *erode* operation with a parameter of 10 were necessary to successfully separate all particles of the NCA/LCO-E cathode. Elements remaining in database 2 were assigned manually in the

end, as a visual inspection showed them to be already separated single particles.

The iterative procedure for the automated separation of particles is done in MATLAB (The MathWorks, Version 2019b, Natick, MA, USA). The final database 3 contains a total of more than 1100 particles from all four cathode reconstructions selected, as explained earlier.

As an additional benefit of the separation process and the fact that the particles are now separated, an even more detailed analysis of the structure can be performed. As all extracted particles are available as matrix in a voxel-based representation, it is easy to calculate characteristic parameters for the particles, such as the average particle volume V , surface area A , particle-to-volume ratio $\frac{A}{V}$, or the sphericity.^[27,28] All these parameters were calculated and are listed in Table 2, separated for all four analyzed cathodes.

The CB phase is the electronically conductive network within a technical cathode structure. The opening procedure had to be adapted to the specific features of the CB phase, especially because the nano-sized CB particles itself are mostly clustered to elongated microporous agglomerates.

Analogous to the procedure explained earlier, a binary matrix is created from the same segmented 3D reconstruction. But now,

Table 2. Geometric characteristic parameters calculated from a representative set of accepted AM particles extracted from the four cathode templates.

Cells	NCA/LCO-E			NCA/LCO-P			LCO-E	NCA-P
Voxel size adapted [nm]		70		70			70	70
Cathode AM	NCA	LCO	all	NCA	LCO	all	LCO	NCA
Number of particles	316	47	363	179	33	212	156	622
Average volume V [μm^3]	18.00	87.54	27.04	9.91	56.83	17.21	63.06	6.04
Average surface A [μm^2]	26.85	105.96	37.09	22.16	79.97	31.16	90.69	23.39
Average $\frac{A}{V}$ [μm^{-1}]	9.88	3.47	9.05	7.65	4.64	7.18	4.57	36.00
Average $\sqrt[3]{\frac{A}{V}}$ [μm^{-1}]	2.72	2.60	2.71	2.71	2.61	2.70	2.76	6.25
Sphericity	0.67	0.73	0.68	0.67	0.72	0.68	0.65	0.24

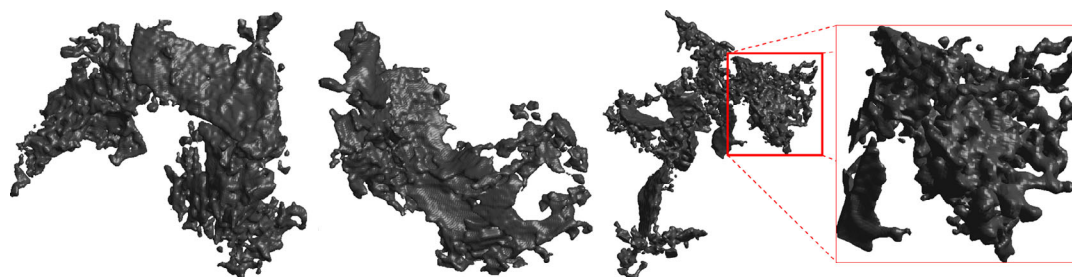


Figure 5. Three examples of CB agglomerates extracted from the CB network by erode operations and stored in the CB library list.

the CB phase is treated as foreground, whereas all other phases are background.

By applying the *erode* operation, the geometrically weak connections of the CB network open first. The size of the erode operation parameter necessary to split up the connection depends on the size of the connections and the data resolution. By optical inspection, it was then assured that the disconnected CB agglomerates are still similar to the original ones, as well as that the calculated particle sizes and surface areas of both types are very similar.

The crucial question is which is a suitable size of CB agglomerates in relation to the AM particle size? If the CB agglomerates are too large, some pore areas in the virtual microstructure will be filled with CB, whereas others might remain without any. If the agglomerate size is improperly chosen, the typical agglomeration of CB is not reflected well in the virtual structure.

Figure 5 shows three exemplary CB agglomerates of the CB library. All conductive CB agglomerates that were extracted for the CB library are rather large (with a size of between 90 000 and 250 000 voxels at a resolution of 70 nm) and consist of several hundreds of primary CB particles. This size was found to be ideal, because the structures generated with it are very similar to the original structures. In total, 20 agglomerates are currently stored in the library, which is sufficient for generating digital twins of our cathode (see Section 3.3 and 4). Nevertheless, the CB library will be expanded in the future by the analysis of further templates. Other methods of splitting the CB network, such as cutting out cubic, spherical, or elliptical structural elements from the CB network, yielded less favorable results.

3. Generation of Virtual Electrode Microstructures

The final libraries with together more than 1100 NCA and LCO particles as well as about 20 CB agglomerates, obtained from processing the four template structures, are now available. First of all, we aim to generate a virtual twin of the NCA/LCO-E cathode template. The workflow is easily adaptable to only one, or more than two AMs.

3.1. Model Step 3: Definition of Virtual Microstructure Characteristics

At the beginning, the desired volume dimensions (number of voxels and voxel size) are specified, with the *x*-direction representing the thickness or the height of the cathode structure,

and *y*- and *z*-directions representing the base area of the cathode. The selected particle list contains as many particles, as are required to achieve the desired AM fraction. Each particle size is numbered according to the arbitrary given particle-size distribution. The same procedure is applied to the CB phase.

3.2. Model Step 4: Placement of AM Particles by Dropping and Rolling

The virtual microstructure is generated using “dropping and rolling” methods.^[29] The randomly picked particles are dropped one after the other into a dimension-specified box, and their final position is derived from a simplified physical process of particles falling into a box. Considering all physical interactions between the particles would be computationally intensive and disproportionately complex. Instead, a method for the particle placement without solving physical laws was implemented, yet calculating a stable final position of the particles.

Model steps 3–5 are implemented in MATLAB and essentially consist of the following sequence. 1) Defining desired volume, material portions, and particle-size distribution: selection of a representative set of AM particles and CB agglomerates. 2) Sequential placement of randomly picked AM particles into a predefined volume box by a “dropping and rolling” approach. 3) Stochastic placement of CB agglomerates in the pore space.

The random starting position of each AM particle is on top of the volume box, and the final placement depends on the continuous adjustment of the particle position following dropping and rolling principles. As shown in **Figure 6a**, the particles are dropped into the box (increasing the *x*-components of all entries of the particle in the volume matrix), until a collision with another particle occurs or the particle reaches the bottom of the box. If a collision is detected, the algorithm rolls falling particles around already placed ones, as schematically shown in **Figure 6b**. Therefore, the particles are moved laterally away from the point of contact, but with the requirement that the movement is not exclusively lateral, but also at least slightly downward (increasing the *x*-component by at least 1, while increasing the *y*- and/or *z*-components by 1–10). Due to the matrix grid representing the voxel-based microstructure, only discrete shifts can be performed. Hereby, 32 shifting directions exist. The shift is only accepted, if it triggers no additional collision. Otherwise, the length of the attempted shift is gradually increased.

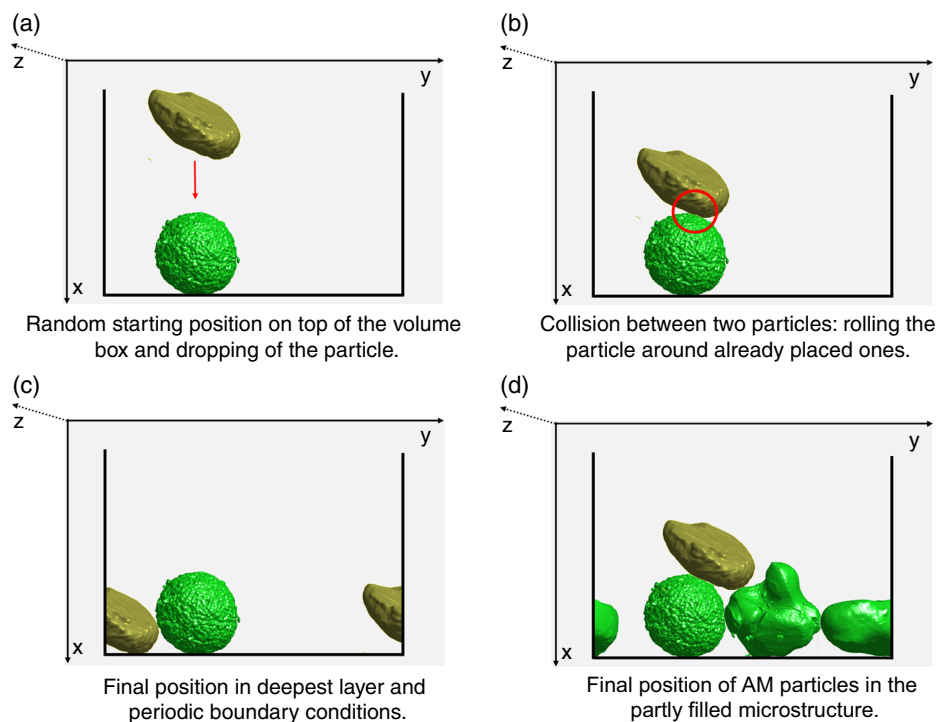


Figure 6. Schematic representation of the placement of AM particles by the dropping and rolling method into a predefined volume box.

Particle sticking is prevented by an additional rotation of the particle with an angle of $\pm 90^\circ$ around all axes in both directions if no shift is possible in its current orientation. The algorithm analyzes the area of contact between the neighboring particles and calculates an averaged point of touch of all voxels. Using this information in addition to the center of gravity, the respective rotation direction is triggered. After rotating the particle, it again tries to roll it around the already placed particles to resolve the collision.

The collision algorithm ends either if the collision is successfully solved, or if every shift (after two rotation steps) would lead to a new collision. In the latter case, the particle has reached a stable final position (see Figure 6d). A particle position is considered stable, if it has at least three supporting points (contacts) to other particles (or if it reaches the bottom of the volume box). These supporting points must be on the bottom side of the particle, the points are not supposed to be on a straight line, and the projection of the particles center of gravity lies within the lower contact surface. In case of a successfully solved collision, the current position is saved, and the algorithm continues with vertically dropping the particle, while trying to reach the bottom of the microstructure (or until a new collision is detected). If a particle reaches the bottom of the box, a final horizontal shift is made in y - z , so that the particles move closer together and no undefined distances between the particles reduce the desired AM content. In reaching a random end position, the shift ends outside the center of the structure (see Figure 6c).

Material depletion or undesirable boundary effects are prevented by periodic boundary conditions at the lateral edges of the box, as shown in Figure 6d. This means that all voxels of

a particle that are shifted out of the box are automatically shifted to the opposite side of the volume box. The four vertical edges, therefore, do not constitute a limitation for the particle shifts. Periodic boundary conditions are also advantageous, if a virtual microstructure is used for electrochemical simulations as the size of the representative volume elements (RVE) is minimized.^[20]

Naturally, the irregular (“true”) shape of all AM particles poses an extra challenge on the dropping and rolling process. The volume box cannot be packed as dense as with perfectly shaped spheres. The particles are restricted to the voxel grid, and therefore, no arbitrary rotations are possible to adapt the different particle shapes to each other and achieve a higher packing density.

The predefined AM fractions are achieved only, if the following side conditions are considered. First, the volume box must have a sufficiently large base area, which should be at least seven times larger than the particle size.^[20] For the described virtual NCA/LCO cathode, with a maximum particle diameter of around $4.65 \mu\text{m}$, a base area of at least $32.6 \mu\text{m} \times 32.6 \mu\text{m}$ ($= 465 \times 465$ voxels) is necessary. Second, the permitted overlap between several particles before a collision is detected plays a dominant role. The permitted overlap can be determined as a total number of voxels applied for all particles, or in relation to the volume size of the falling particle. It is set to 0.3% of the particles volume size here. The material share in the total volume can be increased by increasing the permitted overlap.

Third, toward the end of the dropping and rolling procedure, the limited free space available inhibits the placement of large particles. As the generator discards particles after several unsuccessful placement attempts, it is more likely to have smaller particles in the upper part of the volume box. To ensure

a homogeneous filling of the desired cathode volume, an additional buffer space is added on top, so that the height of the volume is chosen higher than the finally desired height. This buffer volume has to be higher than around 1.5 times the height of the largest particle. The placement of AM particles is finished if no more particles can be placed within the desired cathode volume (volume without buffer volume), or until all particles from the particle list have been placed. After finishing the placement process, the buffer layer is deleted, and the structure is saved at the desired height. This virtual twin volume contains roughly 900 AM particles, which meet the desired AM fraction of 58%.

Due to statistics, virtual structures generated with identical parameters always contain slightly different characteristics, as particles are randomly picked and placed. This will be further investigated in Section 4.

3.3. Model Step 5: Stochastic Placement of the CB Phase

After the AM placement, the CB agglomerates from the CB library are placed stochastically in the remaining pore space of the microstructure. A dominant role for the realistic placement plays the attainable electronic conductivity of the CB phase.

The AM particles in the virtual twin must be covered with the CB phase similar to the 3D template obtained from FIB/SEM tomography. Therefore, the placement of a CB agglomerate is only accepted, if its overlapping area with the neighboring AM phase is above a certain threshold. In our case, an overlap of 5000 voxels was chosen for the virtual cathode, because this matched the NCA/LCO template in an ideal way. During the CB placement, every voxel that is already assigned as AM remains AM (overlapping entries of the CB agglomerates are ignored), and only voxels that were previously assigned as pores will be overwritten. If the randomly selected position of the CB agglomerate does not have sufficient overlap, a new position is selected until this criterion is met. This process is repeated until the desired CB fraction is reached. For duplicating the template microstructure, e.g., roughly 700 CB agglomerates were picked to reach the desired 17% of CB. The resulting generated virtual microstructure is shown in Figure 7, and the predefined geometric values as well as the parameters chosen for their creation are summarized in Table 3.

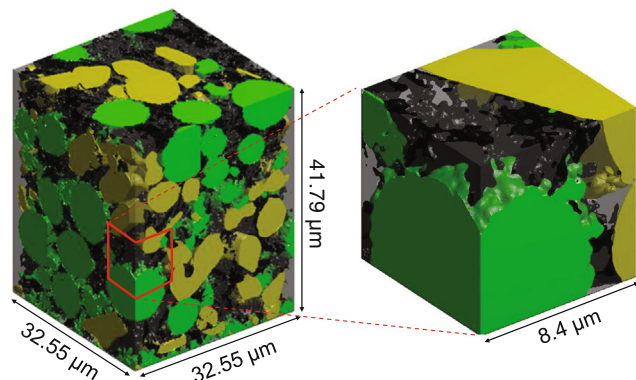


Figure 7. Virtual twin created with predefined microstructure characteristics taken from the template NCA/LCO-E cathode (NCA in green, LCO in yellow, CB in black, and the pore phase is transparent gray).

Table 3. Main characteristics and input parameters used to generate a virtual twin of the template NCA/LCO-E cathode.

Characteristics	Virtual NCA/LCO-E
Base area [μm^2]	32.55×32.55
Cathode thickness [μm]	41.79
Buffer height [μm]	28.21
Voxel size [nm]	70
Particle-size distribution	as cathode NCA/LCO-E
Permitted particle overlap [%]	0.3
Maximum particle volume [voxel]	3.0×10^6
Desired AM fraction [%]	56.86
Desired CB fraction [%]	17.08
Desired Pore fraction [%]	26.06
AM particles	≈ 900
CB agglomerates	≈ 700
Hardware	Intel i5 2500 k@3.7 GHz
Computing time [h]	7

4. Results and Discussion

The generated virtual twin mentioned earlier is now compared with the 3D FIB/SEM template, first qualitatively by optical inspection, and second quantitatively by comparing geometric features, such as material fractions, surface areas, particle-size distributions, and so on.

4.1. Virtual Twin Versus FIB/SEM Template Cathode: Validation by Optical Inspection

The main features and microstructure characteristics of the 3D FIB/SEM template should be met by the virtual twin as close as possible. Figure 8 visualizes both 3D volumes as well as 2D cross-sectional images at the front, center, and back position. The front and back position 2D image of the virtual twin confirms the correct implementation of the periodic boundary conditions, as both are almost identical. This is, of course, not the case for the front and back positions of the FIB/SEM template. The front and back position of the virtual twin show less CB at left and right margins of the image compared with the middle position. This is due to the fact that the periodic boundary condition is implemented only over the sides of the box, but not over the corners. Therefore, a placement in the corners is less likely, which influences an area of about $1 \mu\text{m}$ distance from the corners. However, if looking at the overall behavior of the digital twin structures, this effect is negligible.

The cross sections show a random distribution of large and small particles of the AM phases NCA (green) and LCO (yellow), a good coverage of NCA and LCO particles by CB agglomerates, and a random distribution of the CB agglomerates themselves. However, the optical inspection of the 2D SEM images cannot prove the grade of similarity between template and virtual cathode. The virtual cathode gives the impression that the AM proportion is slightly lower compared with the template cathode

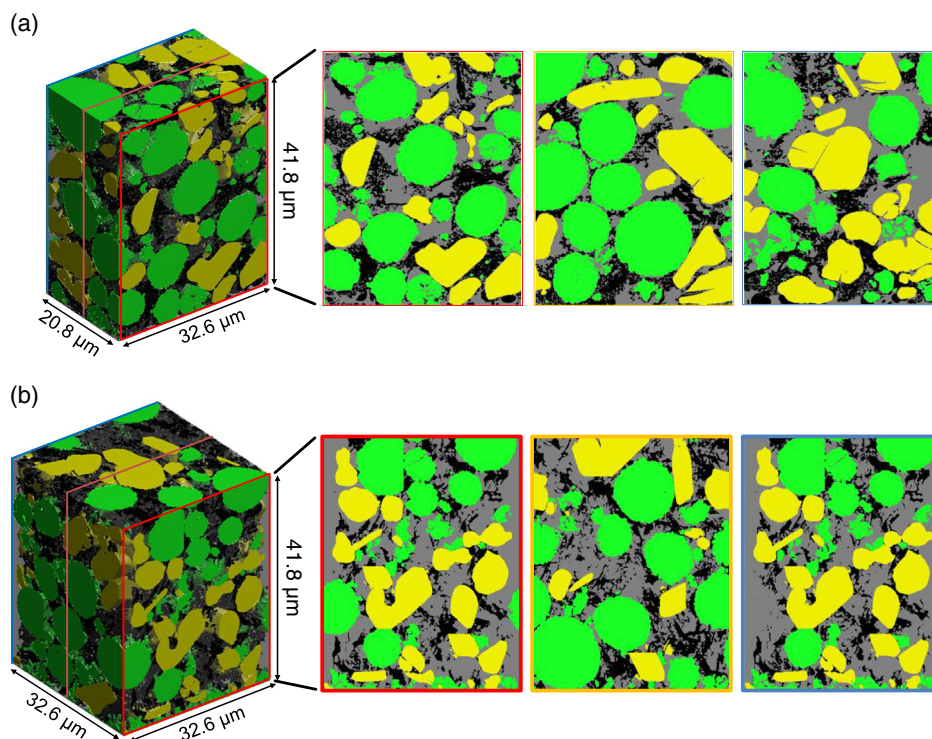


Figure 8. Optical comparison of the a) FIB/SEM derived template NCA/LCO-E cathode and b) virtual twin.

(as analyzed in the following, the template cathode contains: 32.79% NCA and 24.07% LCO; the virtual cathode contains: 32.76% NCA and 20.58% LCO) with a slightly smaller size distribution. Some areas in the lower part of the virtual cathode structure contain more small AM particles due to their higher mobility in the placement process.

4.2. Virtual Twin Versus FIB/SEM Template Cathode: Validation by Quantitative Comparison

First, we checked the homogeneous distribution of all phases. For this purpose, **Figure 9** shows the volume fractions for NCA, LCO, CB phase, and pore phase over the cathode height (x -direction), comparing the virtual twin (dashed lines) with the template cathode (full lines). Hereby, the bottom of the structure is at the origin of the x -axis, and the top is at 41.79 μm , whereas the phase fractions are averaged over the voxel layers (y - z -direction) at each point. In our view, the differences are not significant, and no accumulations of particles, pores, or CB along the cathode thickness are observable. The AM fractions vary by a maximum of around 25% caused by the individual particle arrangement in both inspected cathode volumes. At the bottom, the pore fraction seems to be slightly higher in both structures. In case of the template cathode, this was the separator side. In case of the virtual twin, this was expected, as the bottom of the volume box is the limit for the dropped particles, because only the first ten voxel layers were deleted. If this effect is to be avoided, more voxel layers can be cut off at the bottom, i.e., up to the level of the average particle radius.

The CB phase in the virtual cathode is more homogeneously distributed over the cathode thickness, whereas for the template cathode, a higher amount of CB is in the region near the separator. If desired, this can also be imitated in the virtual cathode, because the CB content can be predefined for any area by the software.

Second, for a closer look on the size of the particles, the number-weighted as well as the volume-weighted particle-size distributions of NCA and LCO are plotted in **Figure 10**. As discussed before, the particle-size distributions play an important role in generating the virtual twin. On the horizontal axis, the particle diameter as calculated by the EDT (explained in Ender et al.^[23]) in μm is displayed, whereas on the vertical axis, the relative proportion in relation to the number (left) and the volume (right) is given. The bars framed in red represent the template cathode, the ones framed in blue the virtual one, whereas the green part of the bars represents the NCA fraction, and the yellow bars represent the LCO.

At first glance, the shape of the number-weighted particle-size distributions matches very well. Both the NCA and the LCO AM particles of the virtual cathode show a slight excess of small particles, which was already assumed from visual inspection of the cross-sectional images (see **Figure 7**). Also the maximum occurring particle size of both cathodes shows a good match, which is also applicable in the volume-weighted particle-size distribution. There one can see that the largest particles are NCA particles, and that even one or two particles of that size can show a noticeable difference in the volume-weighted particle-size distribution. Due to the lack of larger particles (NCA and LCO) in the virtual twin and the overall slightly too low AM

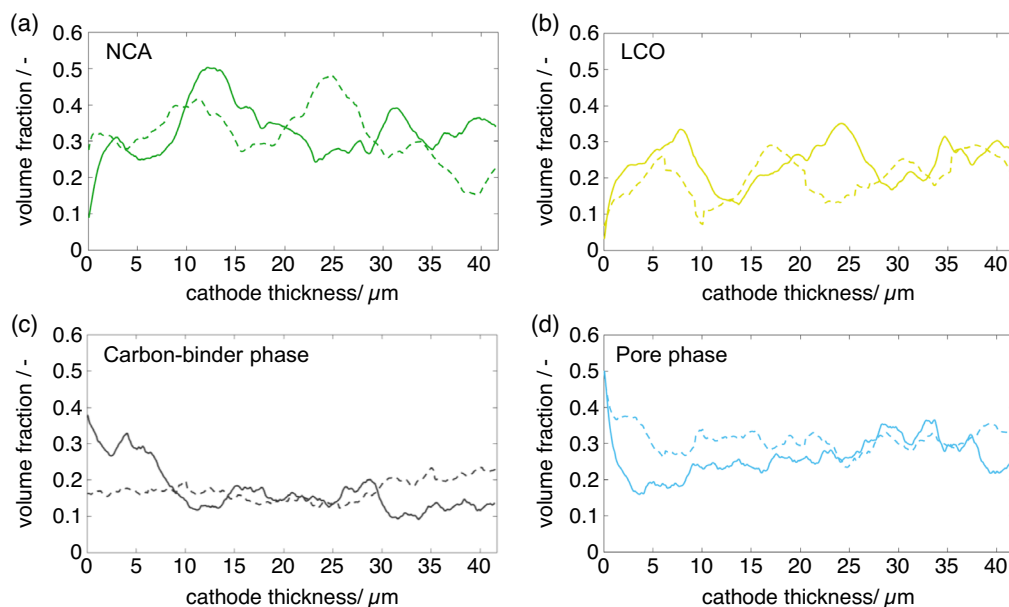


Figure 9. Distributions of the volume fractions for all phases over the cathode height, comparing their distribution within the virtual twin (dashed lines) and the template NCA/LCO-E cathode (full lines).

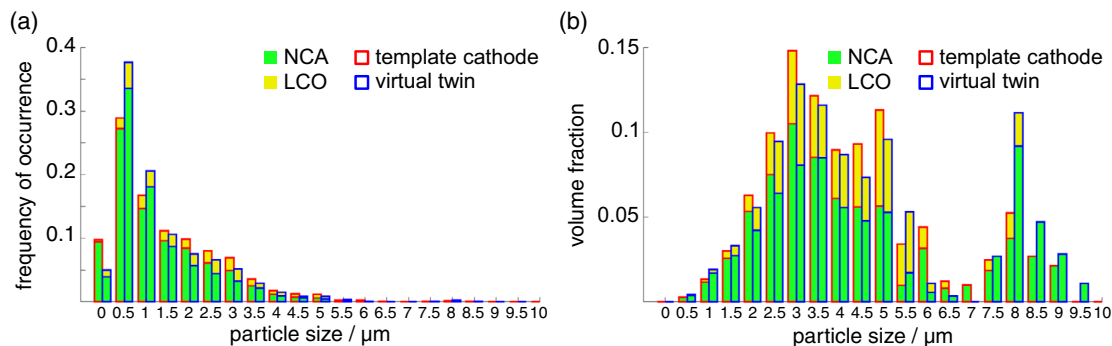


Figure 10. a) Number-weighted and b) volume-weighted particle-size distribution of NCA and LCO in the template cathode (blue framed) and in the virtual twin (red framed).

fraction, the virtual twin seems to have more small particles, according to the EDT.

Third, we quantitatively compare the essential geometric parameters, such as material fractions, surface areas, particle-size distributions of the AMs as well as the CB phase, and the tortuosity of the pore phase. Due to the processes described earlier for picking and placing the particles and agglomerates, statistical deviations of the virtual structures occur, even if these structures are generated with identical input parameters. In the following, the stability of model steps 3–5 is checked regarding these statistical deviations. Therefore, 30 virtual twins were generated with the same input parameters (listed in Table 3). So, the differences are a slightly different list of selected particles to be placed, which is generated anew for each virtual twin, as well as the order of the particles picked and their random placement. All virtual twins were quantified, and the average value was calculated from the results for all parameters, together with their standard deviations, as listed in Table 4.

The average AM fraction (NCA + LCO) of the 30 virtual cathode structures is a little lower with 53.0% compared with 56.8%

in the template cathode. This goes hand in hand with a slightly higher porosity, meaning that the developed algorithm could not place as much AM particles as needed to achieve the desired AM fraction. To increase the AM fraction, i.e., the permitted particle overlap of 0.3% can be increased

The material fraction of CB in the virtual cathode, however, corresponds exactly to the predefined specification. This is understandable, because the very small CB agglomerates are allowed to be placed with high flexibility until the desired volume content is reached. Furthermore, the standard deviations show the scatter of each parameter when generating a virtual cathode with our approach. The standard deviations for all phases are surprisingly low with ± 0.0248 for NCA and ± 0.0216 for LCO and even lower for the pore phase (± 0.010) and the CB phase (± 0.001). These numbers clearly prove the high probability that virtual cathode structures created with the same input parameters will have similar phase fractions.

This also applies to the other parameters, such as the average volume-specific surface areas of all phases. For the surface areas,

Table 4. Microstructure parameters of the template NCA/LCO-E cathode, together with the average values and standard deviations of the 30 virtual twins.

Phase		NCA	LCO	CB	PORE
Average					
Phase fraction [%]	Template	32.81	24.02	17.11	26.05
	Average value (30)	29.63	23.34	17.09	29.94
	Standard deviation	±0.0248	±0.0216	±0.001	±0.010
Surface area [μm^{-1}]	Template	0.43	0.28	1.41	1.94
	Average value (30)	0.47	0.32	1.43	1.63
	Standard deviation	±0.028	±0.027	±0.018	±0.024
Average particle size (num. weighted) [μm]	Template	1.32	2.28	0.41	0.44
	Average value (30)	1.02	1.66	0.41	0.51
	Standard deviation	±0.062	±0.061	±0.002	±0.008
Average particle size (vol. weighted) [μm]	Template	4.27	4.28	0.76	1.80
	Average value (30)	5.06	3.84	0.78	1.67
	Standard deviation	±0.405	±0.297	±0.011	±0.145
Tortuosity [–]	Template	–	–	–	4.3
	Average value (30)	–	–	–	3.8
	Standard deviation	–	–	–	±0.20

the standard deviations are only between 0.018 and 0.028 μm^{-1} . The absolute values also correspond very well in both structures, as the average values are only slightly too high in the virtual structure for the AMs (0.47 μm^{-1} instead of 0.43 μm^{-1} for NCA; 0.32 μm^{-1} instead of 0.28 μm^{-1} for LCO) and the CB (1.43 μm^{-1} instead of 1.41 μm^{-1}). This indicates that the permitted overlap of 0.3% of the particle volume and the particle-size distribution was chosen well.

The latter point is also supported by comparing the average particle size of the different phases. The larger volume-specific surface areas, however, also indicate a smaller (number weighted) average particle size for the AM particles, which is shown in Table 4. Nevertheless, the standard deviations are relatively low for the number-weighted particle and pore size (between only ±0.002 and ±0.062). For the volume-weighted particle sizes, the standard deviations are higher, at least for the two AMs (±0.405 for NCA and ±0.297 for LCO), because the difference increases, if even one more large particle is placed (randomly) inside the considered volume or not. Nevertheless, these standard deviations are still low enough. The standard deviations for the CB and pore phase are relatively small for all cases.

Looking at the tortuosity (defined as in, e.g., the previous study^[13–15], which in literature is often denoted as tortuosity factor), it must be stated that the calculation of the tortuosity only makes sense for the pore phase (and with some restrictions also for the CB), because the AMs do not have to form a 3D network. For 30 virtual twins, the tortuosity of the pore phase was calculated to an average value of 3.8 (standard deviation ±0.20), which is lower compared with 4.3 for the template cathode. This deviation arises from the difference in porosity, which is 29.94% for the virtual twins compared with 26.05% for the template cathode. Overall, the agreement is still reasonable. The comparative value, calculated by the Bruggeman method, is significantly lower with a tortuosity of 1.83 at a porosity of 29.94% ($\tau_{\text{pore, Brugg.}} = \epsilon^{-0.5}$).^[30,31] In addition, the tortuosity of pore phase and CB phase as a single,

joint phase ($\tau_{\text{pore} + \text{CB}}$) was calculated with an average value of 1.6 (standard deviation ±0.029), which is quite close to the value of 1.7 calculated for the template cathode. The comparison with the tortuosity of only the pore phase with 3.8 and 4.3, respectively, is quite large and reveals that an accurate identification of the CB phase is extremely relevant if the tortuosity values are to be used for modeling and simulation,^[15] even if many groups extract only $\tau_{\text{pore} + \text{CB}}$ from their LIB cathode reconstructions, as the contrast between CB phase and pores is too weak.^[1,15–17]

In summary, it can be concluded that the new approach for the generation of virtual twins is valid. This opens the pathway to a variety of virtual cathode designs with specified characteristics, such as mass contents of AM, conductive phase, and pore space, particle-size distributions, and gradients thereof. Naturally, these virtual structures, if coupled to a physics-based electrochemical 3D model with separated and spatially resolved phases (see, e.g., Schmidt et al.^[6]), deliver new insights into structure–performance interaction. Currently, variations with respect to differently distributed AM and CB phase, different cathode thickness and tortuosity, or multi-layered structures with finer and coarser AM particles are in preparation.

5. Conclusion

This work presented a recently developed method for the generation of a virtual, yet true-to-life cathode microstructure. Its precondition is a 3D template of a commercial cathode, which was reconstructed via FIB/SEM tomography and appropriate algorithms. Next, the characteristically shaped, micrometer-sized AM particles and the nano-sized CB agglomerates were individually cut out of the voxel-based 3D volume. This task was performed by morphological operations. Thereby, library lists from four different cathode templates (NCA, LCO, and two blends thereof) were created, with roughly 1100 AM particles

and 20 CB agglomerates. The microstructure generator is based on a matrix grid representing the voxel-based microstructure and applies three sequential steps: 1) Definition of material portions and particle-size distributions; 2) sequential placement of AM particles in a dimension-specified box; and 3) stochastic placement of CB agglomerates into the remaining pore space. Each individual CB agglomerate must overlap with the AM above a given threshold, thus ensuring a certain surface coverage. The randomly selected position of the CB agglomerate is changed until this criterion is met, and thus, the desired electrical conductivity value is well reflected.

To validate our approach, a virtual twin was created of a commercial blend cathode made of the AMs NCA and LCO. A comparison of well-selected microstructural parameters of the virtually generated structure and the (true) 3D cathode template showed an excellent agreement. Moreover, the variances of these parameters were checked by generating 30 structures with identical specifications. The low variances in all parameters indicate a very high reproducibility of the virtual twins with pre-defined microstructural characteristics.

With this new approach, it is possible to create virtual twins of existing cathode structures as well as structures with arbitrary custom-tailored, yet realistic characteristics, thereby overcoming simplifications such as spherical or ellipsoidal particles or a homogeneous distribution of the CB phase. We assume that using “true-to-life” AM particles and CB agglomerates in 3D microstructure models is advantageous for more realistic simulation results of physics-based electrochemical 3D models. Hopefully, advantageous structural properties will be more accurately identified, i.e., for cathode structures from high-energy or high-power cells or a combination thereof.

Acknowledgements

The authors would like to thank Frederik Struckmeier for his invaluable support of this work. Jake Packham supported them by proofreading abstract, introductions, and conclusions, which was gratefully acknowledged. This work was funded by the Deutsche Forschungsgemeinschaft (DFG) through the projects “Multiskalenmodellierung und numerische Simulation von Lithium-Ionen-Batterieelektroden auf Basis realer Mikrostrukturen” (IV 14/20-1, CA 633/2-1) and in the framework of the research training group SiMET (281041241/GRK2218). Open access funding enabled and organized by Projekt DEAL.

Conflict of Interest

The authors declare no conflict of interest.

Keywords

dropping and rolling methods, focused ion beam/scanning electron microscopy tomography, lithium-ion battery cathode, virtual material designs, virtual twin

Received: October 10, 2020

Revised: December 8, 2020

Published online:

- [1] J. R. Wilson, J. S. Cronin, S. A. Barnett, S. J. Harris, *J. Power Sources* **2011**, *196*, 3443.
- [2] W. Li, J. C. Currie, *J. Electrochem. Soc.* **1997**, *144*, 2773.
- [3] J. Feinauer, T. Brereton, A. Spettil, M. Weber, I. Manke, V. Schmidt, *Comput. Mater. Sci.* **2015**, *109*, 137.
- [4] J. Newman, W. Tiedemann, *AIChE J.* **1975**, *21*, 25.
- [5] M. Ender, *J. Power Sources* **2015**, *282*, 572.
- [6] A. Schmidt, E. Ramani, T. Carraro, J. Joos, A. Weber, M. Kamlah, E. Ivers-Tiffée, *Energy Technol.* **2020**, <https://doi.org/10.1002/ente.202000881>.
- [7] W. Wu, F. Jiang, *Mater. Charact.* **2013**, *80*, 62.
- [8] S. He, J. Zeng, B. T. Habte, F. Jiang, *Sci. Bull.* **2016**, *61*, 656.
- [9] V. Becker, O. Birkholz, Y. Gan, M. Kamlah, *Energy Technol.* **2020**, unpublished.
- [10] S. Cernak, F. Gerbig, M. Kespe, H. Nirschl, *Energy Technol.* **2020**, *2*, e156.
- [11] D. Oehler, P. Seegert, T. Wetzel, *Energy Technol.* **2020**, 2000574.
- [12] D. Westhoff, I. Manke, V. Schmidt, *Comput. Mater. Sci.* **2018**, *151*, 53.
- [13] J. Joos, T. Carraro, A. Weber, E. Ivers-Tiffée, *J. Power Sources* **2011**, *196*, 7302.
- [14] M. Ender, J. Joos, T. Carraro, E. Ivers-Tiffée, *Electrochem. Commun.* **2011**, *13*, 166.
- [15] L. Almar, J. Joos, A. Weber, E. Ivers-Tiffée, *J. Power Sources* **2019**, *427*, 1.
- [16] V. Malavé, J. R. Berger, H. Zhu, R. J. Kee, *Electrochim. Acta* **2014**, *130*, 707.
- [17] T. Hutzenlaub, S. Thiele, N. Paust, R. Spotnitz, R. Zengerle, C. Walchshofer, *Electrochim. Acta* **2014**, *115*, 131.
- [18] R. Moroni, M. Börner, L. Zielke, M. Schroeder, S. Nowak, M. Winter, I. Manke, R. Zengerle, S. Thiele, *Sci. Rep.* **2016**, *6*, 1.
- [19] J. Costard, J. Joos, A. Schmidt, E. Ivers-Tiffée, *Energy Technol.* **2020**, <https://doi.org/10.1002/ente.202000866>.
- [20] J. Joos, M. Ender, T. Carraro, A. Weber, E. Ivers-Tiffée, *Electrochim. Acta* **2012**, *82*, 268.
- [21] J. Joos, M. Ender, I. Rotscholl, N. H. Menzler, E. Ivers-Tiffée, *J. Power Sources* **2014**, *246*, 819.
- [22] W. E. Lorenzen, H. E. Cline, *ACM Trans. Graph.* **1987**, *21*, 163.
- [23] M. Ender, J. Joos, T. Carraro, E. Ivers-Tiffée, *J. Electrochem. Soc.* **2012**, *159*, A972.
- [24] M. Ender, J. Joos, A. Weber, E. Ivers-Tiffée, *J. Power Sources* **2014**, *269*, 912.
- [25] E. H. Van Den Berg, A. G. C. A. Meesters, J. A. M. Kenter, W. Schlager, *Comput. Geosci.* **2002**, *28*, 179.
- [26] S. Zaefferer, S. I. Wright, D. Raabe, *Metall. Mater. Trans. A* **2008**, *39*, 374.
- [27] H. Wadell, *J. Geol.* **1933**, *41*, 310.
- [28] I. Cruz-Matías, D. Ayala, D. Hiller, S. Gutsch, M. Zacharias, S. Estradé, F. Peiró, *J. Comput. Sci.* **2019**, *30*, 28.
- [29] Y. Shi, Y. Zhang, *Appl. Phys. A Mater. Sci. Process.* **2008**, *92*, 621.
- [30] D. A. G. Bruggeman, *Ann. Phys.* **1935**, *416*, 636.
- [31] B. Tjaden, S. J. Cooper, D. J. Brett, D. Kramer, P. R. Shearing, *Curr. Opin. Chem. Eng.* **2016**, *12*, 44.